Evidence of new Ni-O-K catalytic sites with superior stability for methane dry reforming

Lola Azancot [a,*], Vincent Blay [b], Rubén Blay-Roger [a], Luis F. Bobadilla [a], Anna Penkova [a], Miguel A. Centeno [a], José A. Odriozola [a,c]

[a] Departamento de Química Inorgánica e Instituto de Ciencia de Materiales, Centro Mixto CSIC-Universidad de Sevilla, Av. Américo Vespucio 49, 41089 Sevilla, Spain
[b] Biological Systems and Engineering Division, Lawrence Berkeley National Laboratory, Berkeley, CA 94720, USA
[c] Department of Chemical and Process Engineering, University of Surrey, Guildford GU2 7XH, UK

ARTICLE INFO

ABSTRACT

Liquid fuels produced *via* Fischer-Tropsch synthesis from biomass-derived syngas constitute an attractive and sustainable energy vector for the transportation sector. This study focuses on the role of potassium as a promoter in Ni-based catalysts for reducing coke deposition during catalytic dry reforming. The study provides a new structural link between catalytic performance and physicochemical properties. We identify new Ni-O-K chemical states associated with high stability in the reforming process, evidenced by different characterization techniques. The nickel particles form a core surrounded by a Ni-O-K phase layer (Ni@Ni-O-K) during the reduction of the catalyst. This phase likely presents an alkali-nickelate-type structure, in which nickel is stabilized in oxidation state + 3. The Ni-O-K formation induces essential changes in the electronic, physical, structural, and morphological properties of the catalysts, notably enhancing their long-term stability in dry reforming. This work thus provides new directions for designing more efficient catalysts for sustainable gas-to-liquids processes.

1. Introduction

The efficient conversion of biogas to liquid fuels (Bio-GTL) could become a key industrial process in the future bio-economy. Biogas is an attractive renewable energy source and can be produced by anaerobic digestion of organic wastes in the presence of microorganisms. Methane and carbon dioxide are the major constituents of biogas, although traces of ammonia, hydrogen, oxygen, hydrogen sulfide, water vapor and other impurities can be present depending on the feedstock used (landfill, sewage sludge, agricultural waste, *etc.*) [1]. Although biogas can have different uses [2], its high concentration of CO_2 and CH_4 makes it ideal for syngas production by dry reforming with minimal purification. Syngas is a CO and hydrogen-rich gas mixture that can be readily converted to high-performance liquid fuels by the Fischer-Tropsch process [3,4].

The catalytic reforming of biogas has been widely studied for the last two decades. Currently, the main limitation to industrialize this technology is the low catalytic stability associated with coke deposition and metal sintering under reaction conditions. Owgi et al. [5] surveyed different catalytic systems for the dry reforming of methane, analyzing

the effect of active metals, support materials, promoters, and preparation methods, and concluded that the design of cost-effective and stable catalysts for biogas reforming is an unsolved challenge. Recently, significant progress has been made in understanding catalysts under working conditions using *in situ* and *operando* techniques [6–8]. The investigation of catalysts under realistic conditions allows correlating the dynamic structural changes of the catalyst surface in the presence of reactants with catalytic performance [9], providing unique insights that could inform the rational design of better catalysts.

Nickel catalysts are favored in industrial applications for their low-cost. Different strategies are used to control the nickel particle size and mitigate coke deposition, such as the use of basic supports and doping of the catalyst with alkaline metals, which enhances the metal dispersion and favors coke gasification by the reverse Boudouard reaction [10,11]. Indeed, the addition of potassium as a promoter on nickel catalysts has been extensively investigated. However, the role of potassium in Ni-based catalysts during reforming is not fully understood. Borowiecki et al. [12] proposed that the effect of potassium as a promoter is directly related to its location and chemical state on the catalyst surface. They showed that only those potassium atoms close to nickel

sites promote gasification of carbonaceous deposits produced in methane cracking. Frusteri et al. [13] suggested that potassium induces an electronic effect on Ni/MgO catalysts, inhibiting the rate of coke formation, carbon nucleation, and carbon diffusion through the nickel sites. In a previous study, we reported that introducing a potassium promoter on a Ni/MgAl$_2$O$_4$ catalyst changed the nature of the catalytic active sites and enhanced their coking resistance [14]. We proposed that the existence of Ni-K containing phase favors the gasification of carbonaceous deposits by the reverse Boudouard reaction and reduces the sticking probability of CO/CO$_2$ in dissociative adsorption.

At present, several questions about the effect of potassium in dry reforming remain unsolved, which limit our ability to design better catalysts. *Where is the potassium located on the catalyst? What properties of the material are affected? Is potassium a carbon gasifier?* In this work, we investigate how the addition of potassium affects the structural properties, reducibility, and chemical state of Ni-based catalysts, as well as its relationship with the catalytic activity and stability in the dry reforming of methane. To this end, we study a series of xK-Ni/MgAl$_2$O$_4$ catalysts with identical amounts of nickel but different potassium loads (x between 0 and 5 wt%). The study includes a combination of *in situ* X-ray diffraction (XRD), X-ray photoelectron spectroscopy (XPS), temperature-programmed reduction (TPR), and diffuse reflectance infrared Fourier transform spectroscopy (DRIFTS) coupled with mass spectrometry (MS) to investigate the structural and redox changes occurring during the dry reforming of methane.

2. Experimental section

2.1. Catalysts synthesis

The support, a stoichiometric aluminium magnesium spinel (MgAl$_2$O$_4$), was synthesized by co-precipitation and treated at 900 °C for 24 h following a previously described procedure [15]. The solid obtained was labelled as MgAl.

The catalysts were prepared by wet co-impregnation of potassium (KNO$_3$) and nickel (Ni (NO$_3$)$_2$·6H$_2$O) salts. Adequate amounts of these salts to obtain 1, 3 or 5 wt% potassium and 10 wt% nickel loading were diluted in water and mixed with the support. Excess water was removed by roto-evaporation at 60 °C. The samples obtained were dried overnight at 100 °C (fresh catalysts) and then calcined at 550 °C for 4 h (calcined catalysts). The catalysts were designated as xK-Ni/MgAl, where x indicates 1, 3 or 5 wt% of K$_2$O. For comparison, an unpromoted catalyst was also synthesized by impregnating the bare support with the nickel salt solution and designated as Ni/MgAl.

2.2. Characterization techniques

For every characterization study, a calcined sample of catalyst from the original synthesis batch was used, except for those techniques using spent catalysts.

Nitrogen adsorption-desorption experiments of the calcined catalysts were carried out in Micromeritics Tristar II instrument to evaluate their textural properties. Prior to measurement, the samples were outgassed in vacuum at 250 °C for 4 h. The specific surface area and pore volume were estimated using the Brunauer-Emmett-Teller (BET) and Barrett-Joyner-Halenda (BJH) models, respectively.

UV–Visible spectroscopy characterization of the calcined catalysts was carried out in a Shimadzu 2101 spectrometer with a diffuse reflectance accessory. The electronic spectra were recorded in the wavelength range from 190 nm to 900 nm. The bandgap energies were estimated from the intercept of the tangents to the plots of $(\alpha * h\nu)^{1/2}$ against the photon energy [16].

In situ X-ray diffraction and reducibility analyses of the calcined catalysts were performed in a high-temperature chamber Anton Paar HTK 1200 coupled with an X'Pert Pro Philips diffractometer equipped with Ni-filtered Cu Kα radiation (40 mA, 45 kV) and a X'Celerator

detector. The powder XRD patterns were recorded with a 0.05° step size in the 10° to 90° 2θ range and 30 s time steps. Measurements were carried out every 100 °C in the 25–900 °C temperature range while flowing 100 NmL min^{-1} of 5% H$_2$ diluted in argon through the chamber.

XPS measurements of the calcined catalysts were carried out in a SPECS spectrometer equipped with a PHOIBOS 150 MCD analyzer working at fixed pass energy of 40 eV and 0.1 eV resolution for the studied zones. Al Kα radiation (1486.6 eV) was used at 250 W and 12.5 kV. Prior to analysis, each sample was pressed into a thin disk. All XPS spectra were recorded at room temperature with the binding energy calibrated with Mg 2p at 50 eV. The samples were reduced *in situ* at 800 °C during 1 h in 5%H$_2$/Ar mixture in a high-pressure treatment cell (HTHP Cell). After reduction, the evacuation of the gases was maintained overnight before the spectrum was acquired at room temperature under vacuum. The analytical chamber operates under ultra-high vacuum (10^{-10} mbar).

In situ TPR-DRIFTS analysis of the calcined catalysts was performed using a high-temperature environmental reaction chamber with ZnSe windows supported in a Praying Mantis (Harrick) optical system and coupled to a Thermo Nicolet iS50 FTIR spectrometer with MCT detector. The spectra were recorded as an average of 64 scans with 4 cm^{-1} of spectral resolution per spectrum. 80 mg of finely ground calcined catalyst was loaded in the cell for each experiment. The temperature-programmed reduction (TPR) was performed by feeding a flow of 5% H$_2$ in Ar (50 NmL min^{-1}) and increasing the temperature from room temperature to 750 °C at a rate of 10 °C min^{-1}. The spectra were recorded in continuous series mode using the OMNIC 9.1 software and the temperature was simultaneously monitored using a software written in Labview. The effluent gases were analyzed on line by mass spectrometry (PFEIFFER Vacuum Prisma Plus).

A quartz U-shaped reactor fitted in a homemade temperature programmed device equipped with a TCD detector was used to analyze the reduction (TPR) of the calcined catalysts. For the TPR quantitative analysis, the TCD signal was calibrated with a CuO pattern (Strem Chemicals 99.999%). Water and other condensable gases were trapped in a cryogenic bath of dry ice and acetone. An analogous experiment was performed by omitting the cold trap and substituting the TCD by an on line mass spectrometer (Pfeiffer Vacuum Prisma Plus) to monitor the gases evolved during the TPR experiment. The modelling of the TPR was performed using the optimization toolbox in MATLAB 2020a. The modelling involved the numerical optimization of kinetic parameters with the resolution of a system of ordinary differential equations (ODEs), which describes the TCD signal over time (see Supporting Information for details). Prior to modelling, experimental data were conditioned by removing the electric noise of the TCD using a loess filter. Background subtraction was applied using a piecewise cubic Hermite interpolating polynomial. The time window used in the fitting was clipped to that in which reduction processes were observed. The resolution of the system of ODEs was carried out with an adaptive Runge-Kutta algorithm. The optimization started from guess values for the parameters provided manually. The parameter values were then iteratively refined using a combination of Nelder-Mead and Levenberg-Marquardt optimization algorithms to minimize the sum of squared residuals between the experimental TPR signal and the model prediction. The confounding between fitted parameters was assessed by their standard errors, estimated by numerically computing the Jacobian of the objective function at the optimum.

A cold-cathode Hitachi® S4800 SEM-FEG microscope was used for SEM analysis of reduced (800 ºC during 1 h in 5% v/v H$_2$/N$_2$) and spent catalysts. High resolution transmission electron microscopy (HR-TEM) micrographs of reduced catalysts were taken with a Talos® F200S FETEM microscope operated at 200 kV. At least 200 particles were measured to assess the diameter of nickel particles. The volume-surface average diameter was estimated assuming a spherical morphology with the following expression [17]:

$$D_p = \frac{\sum n_i d_i^3}{\sum n_i d_i^2} \tag{1}$$

where n_i represents the number of particles with diameter d_i.

The nickel exposed surface area and the metallic dispersion of the catalysts were estimated by H_2 chemisorption pulses based on the quantity of hydrogen chemisorbed over nickel surface atoms. The experiments were performed in a U-shape quartz reactor loaded with 800 mg of sample. Firstly, the sample was reduced *in situ* at 800 °C under 50 NmL min^{-1} of 5% H_2/Ar for 1 h, and then the temperature was decreased to 60 °C in Ar flow. At this temperature, calibrated volume pulses of 250 μL of pure hydrogen were successively introduced until saturation was achieved, indicating that hydrogen species covered the nickel metallic surface thoroughly. The pulses were monitored from the H_2 signal (m/z= 2) by mass spectrometry (PFEIFFER Vacuum Prisma Plus).

Temperature-programmed oxidation (TPO) experiments were carried out using approximately 50 mg of spent catalysts to analyze the carbon deposits formed in the reforming reactions. The same equipment was used as in the TPR measurements. Samples were heated from room temperature to 900 °C with a rate of 10 °C min^{-1} under 50 mL min^{-1} SPT of O_2/He (10% v/v) flow. The signals of CO_2 (m/z= 44), O_2 (m/z= 32), and CO (m/z= 28) were followed on line by mass spectrometry in a PFEIFFER MS Vacuum Prisma Plus.

A dispersive Horiba Jobin Yvon LabRam HR800 Confocal Raman microscope using a green laser (532.14 nm) working at 5 mW and with a 600 grooves mm^{-1} grating was used to record the Raman spectra of spent catalysts. A 50x objective (Olympus) was used in the microscope with a confocal pinhole of 1000 μm.

Powder X-ray diffraction (XRD) analysis of spent catalysts was performed on a Siemens D-500 diffractometer using a Ni-filtered Cu Kα radiation at 40 mA and 45 kV. The diffraction patterns were recorded in the 2θ range from 10–90° using 0.05° step size and 300 s time steps.

2.3. Catalytic testing in DRM reaction

The catalytic activity in the dry reforming of methane (DRM) reaction was evaluated at atmospheric pressure in a Microactivity Reference (PID Eng & Tech) reactor coupled to a microGC (Varian 4900) equipped with Porapak Q and MS-5A columns and TCD detectors. A fixed-bed tubular reactor of 9 mm inner diameter made of Hastelloy was used for all the experiments. Prior to each test, 200 mg of non-diluted calcined catalyst (sieved to 100–200 μm) was reduced at 800 °C for 1 h in 100 NmL min^{-1} of 50% H_2/N_2. All catalytic tests were carried out at 30 NL g^{-1} h^{-1} space velocity using a molar ratio CH_4/CO_2 = 1 at 650 °C for 48 h. Experiments were performed at three different partial pressures of 20, 30 and 40 kPa for each reactant, using nitrogen to balance the total pressure at 100 kPa.

3. Results and discussion

3.1. Potassium changes the surface structure of Ni-based catalysts: Formation of Ni-O-K layer

Potassium addition leads to a change in the textural properties of the Ni-based materials prepared. Fig. S1 summarizes the textural properties of the materials after calcination. The mesoporous support presents a monomodal pore size distribution peaking at ~20 nm, which remains unchanged upon nickel impregnation. The observed BET specific surface area (S_{BET}) for the support is 83 m^2 g^{-1}. After nickel incorporation, the specific surface area decreases slightly to 71 m^2 g^{-1}, suggesting that nickel gets well distributed throughout the pores of the support. The surface area strongly decreases upon adding potassium to the catalyst (Table S1). This may indicate that, impregnation with potassium leads to reconstruction of the support surface, probably with formation of strong

basic sites [18].

Fig. 1A shows the UV–Vis spectra of the calcined catalysts in the 200–800 nm region. It contains bands of different widths, corresponding to different nickel-support interactions. The undoped Ni/MgAl material presents a broad featureless band centered at ~250 nm, which is associated to $O_{2p}{\rightarrow}Al_{3sp}$ electronic transitions [19]. When increasing the K content above 1 wt%, this band splits in two at 252 and 212 nm, respectively. The splitting strongly suggests that potassium stimulates spinel inversion, modifying the acid-base properties of the support. Spinel inversion is the partial interconversion of A and B sites in the spinel structure, giving rise to oxygen vacancies. The simultaneous addition of K and Ni precursor salts to the spinel support in the synthesis is necessary for Ni ions to participate in the defect creation process. The absorption spectrum also suggests that some nickel ions are incorporated in the spinel structure. Both doped- and undoped-Ni materials present broad bands at 380, 407, 650 and 737 nm, likely associated with Ni^{2+} ions in tetrahedral and octahedral coordination sites [20,21,22]. The low energy bands at 652 and 737 nm (ascribed to $^3T_1(F){\rightarrow}^3T_2(P)$ and $^3T_1(F){\rightarrow}\,^1T_2,^1E(D)$ transitions, respectively) are indicative of tetracoordinate nickel species. This points to the incorporation of nickel ions in the spinel structure (NiAl$_2$O$_4$), since only hexacoordinated Ni^{2+} ions can be accommodated in the rock salt-like structure of NiO. On the other hand, hexacoordinated Ni^{2+} ions in NiO or Ni$_{1-x}$Mg$_x$Al$_2$O$_4$ may account for the bands at 380 and 407 nm. The NiO UV–Vis absorption spectrum is dominated by the valence band (VB) to conduction band (CB) transition at 355 nm, whereas the d-d transition in the visible region is hardly visible [23], in agreement with absorption coefficients previously reported (Table S2). The small shoulder at 380 nm is associated with trapped holes associated with Ni^{2+} species.

The deposition of Ni and K introduces defects (oxygen vacancies) in the spinel support. It was reported that the MgAl$_2$O$_4$ indirect bandgap is 7.8 eV. However, the presence of oxygen vacancies results in interband energy states and an electron transition at 4.75 eV (260 nm) [24]. Solid non-stoichiometry, disorder or impurities may result in complex defects, including the generation of interstitial oxygen atoms and spinel inversion. These defects originate an optical transition at 5.3 eV (230 nm) [25]. Fig. 1B indicates the estimated band gap values for all the calcined catalysts. Notably, the band gap decreases from 3.37 eV in Ni/MgAl sample to 3.24 eV in the case of 5 K-Ni/MgAl. This indicates that potassium doping favors the formation of oxygen vacancies. Wrobel et al. [26] demonstrated that potassium may be incorporated in NiO nanostructures, resulting in hole-doped materials. The presence of defects may result in coordination numbers below six for nickel ions: tetracoordinated [NiO$_4$] polyhedral units (square-planar in K$_2$NiO$_2$ and tetragonal in K$_9$Ni$_2$O$_7$) have been reported, the latter also containing Ni^{3+} ions [27]. Laporte forbidden d-d transitions of Ni^{2+} ions in K$_2$NiO$_2$, characterized by a broad band at ~625 nm [28], cannot be excluded.

The materials prepared may change when they are used under the high temperature and reducing conditions of a dry reforming reactor. To investigate this, *in situ* X-ray diffraction experiments were conducted while exposing the catalysts to increasing temperature under a reducing flow of 5% H_2/Ar (Fig. 2). The results indicate that the phases present initially in the materials are spinel phases (MgAl$_2$O$_4$ and likely some NiAl$_2$O$_4$), nickel oxide (NiO with bunsenite structure), and traces of aluminium oxide. In addition, potassium-rich samples (3 wt% and 5 wt %) also present some potassium nitrate (KNO$_3$). The small amounts of potassium nitrate present in the starting materials are rapidly reduced at 400–500 °C (Fig. 2). Notice that these nitrate species had not decomposed during the oxidative calcination in the preparation of the materials. Virtually no K$_2$O was detected in any measurement.

NiO reduction starts in all samples at 600 °C, which is accompanied by an increase in reflections characteristic of metallic nickel at 2θ values of 44.5° and 51.8° (Fig. 2). The potassium loading does not seem to affect the onset temperature for the NiO reduction process. However, as the temperature is increased, the Ni peaks become sharper and more intense in the 3 K-Ni/MgAl and 5 K-Ni/MgAl. This suggests that metallic
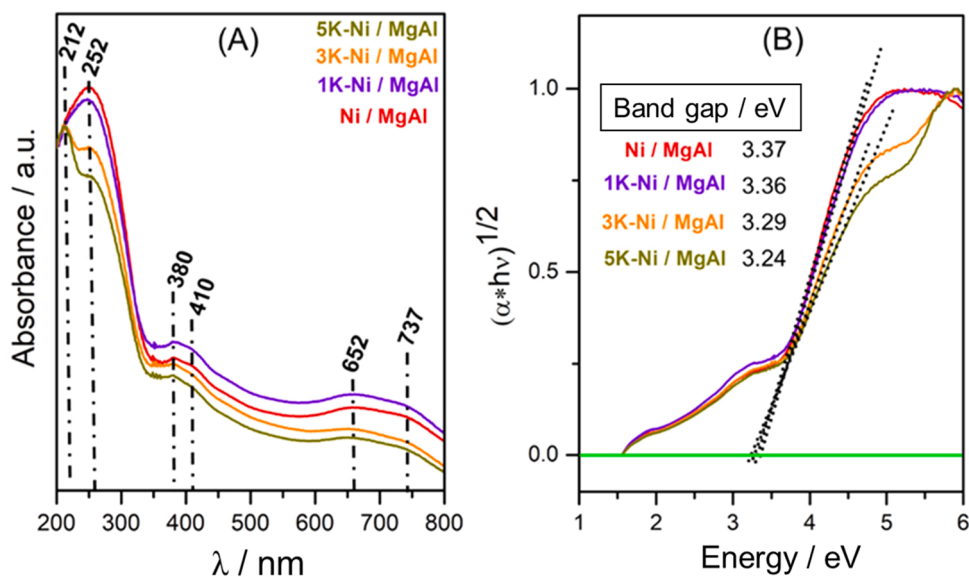
Fig. 1. UV–Vis absorption spectra (A) and plots of (α * *hν*)$^{1/2}$ against photon energy (B) for all the calcined catalysts. The inset in (B) indicates the estimated band gaps.
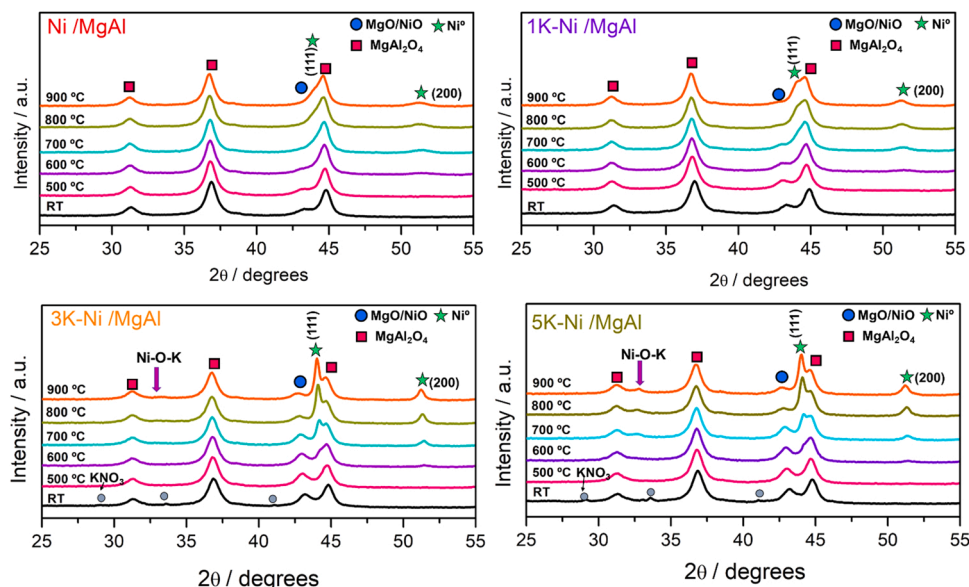

Fig. 2. Evolution of XRD patterns during reduction treatment under 5%H$_2$ in argon atmosphere as a function of temperature for all the calcined catalysts.

nickel sintering may be stimulated by high potassium loading. In agreement with this, Mross reported that the incorporation of alkali ions in the NiO lattice diminishes the activation energy of recrystallization and provokes the sintering of the metal particles [29]. Also, El-Shobaky et al. [30] observed that the incorporation of monovalent ions in the NiO lattice induces the formation defects, facilitating the diffusion of ions in the outermost surface layers and the agglomeration of nickel particles.

Potassium may favor the mobilization of species from the spinel at high temperature. As shown in Fig. 2, in the samples with high loads of potassium, the diffraction peak at 2θ = 42.7°, associated with NiO/MgO phases, persists even at 800–900 °C. This suggests that the incorporation of potassium in the catalyst may promote the migration of Mg^{2+} and Ni^{2+} ions from the bulk spinel lattice to the outer surface layers. We believe that, at temperatures above 600 °C, potassium interacts with nickel particles and helps with the reduction and mobilization of NiAl$_2$O$_4$ and MgAl$_2$O$_4$, leading to higher final amounts of metallic Ni and NiO/MgO oxides. Also note that, in the starting materials, the relative

amount of NiO also increases with the potassium loading, suggesting that potassium may exert a similar mobilizing effect under the oxidant calcination conditions.

Remarkably, in potassium-rich materials (3 wt% and 5 wt%), a new crystalline phase is detected under high-temperature, reducing conditions. As the potassium loading is increased, a new diffraction peak appears at 32.8° at temperatures above 700 °C. The diffractograms at high temperature did not show any crystalline diffraction related to known potassium species, suggesting that K$^+$ cations could have entered the NiO crystal lattice to form a new Ni-O-K structural phase. In more detail, Fig. 3 shows the diffractograms recorded at 800 °C during *in situ* reduction for all catalysts. All the samples lack the peaks expected for the (220), (311), (222), (200), and (400) reflection planes of the MgAl$_2$O$_4$ spinel lattice. Moreover, the (111) reflection of well-crystallized metallic nickel (2θ = 44.5°) is observed in all samples. High potassium loads (3 wt% and 5 wt%) lead to a new diffraction peak at an angle of 32.8°. The assignment of this peak is unclear: it might be
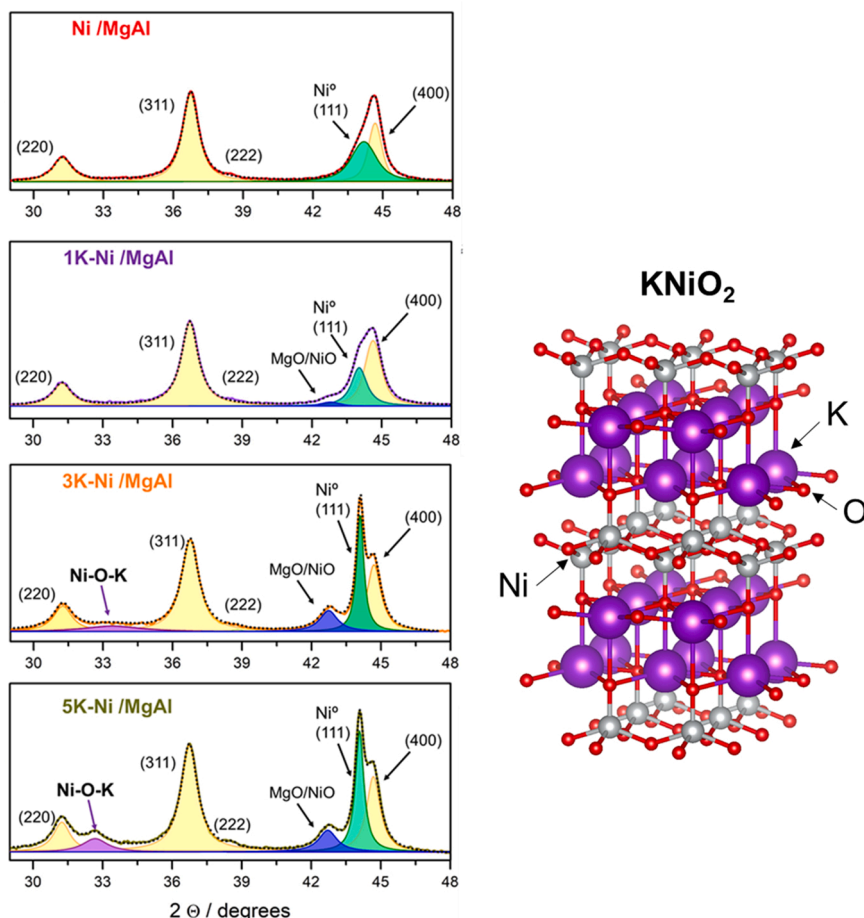
Fig. 3. Selected XRD diffraction patterns at 800 °C for all samples during *in situ* reduction treatment (left) and schematic representation of KNiO$_2$ structure (right).

attributed to the formation of K-Al-O phases or K-doped MgAl$_2$O$_4$ spinel. However, the large ionic radius of potassium would hamper the formation of this type of K-Al-O phases. Considering the UV–Vis analysis discussed above, we tentatively assign these peaks to the formation of nickel potassium oxide composite layers (Ni-O-K).

Praliaud et al. [31] suggested that K is mainly present in the K$^+$ form and that a Ni-O-K surface complex is formed on the surface of nickel particles. The addition of alkali metals on the NiO surface has been extensively studied, and the formation of Ni^{3+} oxidation states in these phases has been proposed to occur by the following reaction:

$$K_2O_2 + 2\,NiO \rightarrow 2\,KNiO_2 \qquad (2)$$

The formation of potassium nickelate phases leads to the stabilization of nickel in the trivalent formal oxidation state. Kim et al. [32] described the KNiO$_2$ structure illustrated in Fig. 3. Interestingly, Ni^{3+} occupies pyramidal sites located between potassium layers with an adequate K-K distance to accommodate the nickel cations, minimizing the electrostatic repulsions between potassium ions. Our results suggest that a new phase, designated as Ni-O-K, is formed during the reduction treatment, which may be compatible with proposals like KNiO$_2$.

XPS measurements were conducted to investigate the electronic state of nickel both in the presence and absence of potassium and confirm the existence of a new phase designated as Ni-O-K that contains nickel in state trivalent. Fig. 4 A includes the Ni 2p$_{3/2}$ spectra recorded for both Ni/MgAl and 5 K-Ni/MgAl samples without treatment and after *in situ* reduction at 800 °C. The two samples show a main peak at 854.1 eV with the corresponding shake-up satellite peak at 860.2 eV. These binding energies are typical of nickel oxide (NiO) disperse on the catalyst surface [33]. Apparently, both unpromoted and K-doped samples

present similar Ni 2p$_{3/2}$ spectra. However, after reduction treatment, notable changes become visible in both samples. XPS analysis of the reduced Ni/MgAl sample indicates the formation of metallic nickel (850.3 eV) and the presence of a weak peak at 857.1 eV, which is related to Ni^{2+} cations in NiAl$_2$O$_4$ spinel. This high binding energy stems from the strong metal-support interaction [34]. By contrast, the reduced 5 K-Ni/MgAl displays a broad peak at 857.1 eV, while the peak assigned to Ni^0 is very faint. The broad peak may be affected by the complex main line splitting due to multiplet contributions in oxides, although its high binding energy and broadening clearly indicate that the oxidation state of nickel is formally Ni^{3+} [35,36]. Different authors have postulated that potassium doping inhibits the reduction of nickel and shifts the binding energy to higher values due to the presence of ionic potassium and the formation of Ni-O-K complexes [31]. Carley et al. [37] investigated the interaction between potassium and nickel single-crystal (100) surface by XPS measurements, evidencing the formation of Ni^{3+} unambiguously after annealing the surface at 600 K. The authors suggested the formation of species between nickel and potassium where the chemical state of nickel is formally + 3. These observations are in good agreement with our results.

The contribution from multiplet splitting, satellite peaks and plasmon loss structures often complicates the interpretation of XPS results, particularly for nickel species in different surface environments. Biesinger et al. [38] reported that additional insights can be obtained from the Ni LMM Auger peak-shape. Fig. 4B shows the Ni LMM Auger spectra for the fresh and reduced samples. The peak-shapes observed in both fresh Ni/MgAl and 5 K-Ni/MgAl samples are typical of NiO species, while the reduced Ni/MgAl sample presents a LMM Auger peak-shape characteristic of metallic Ni. By contrast, the reduced 5 K-Ni/MgAl
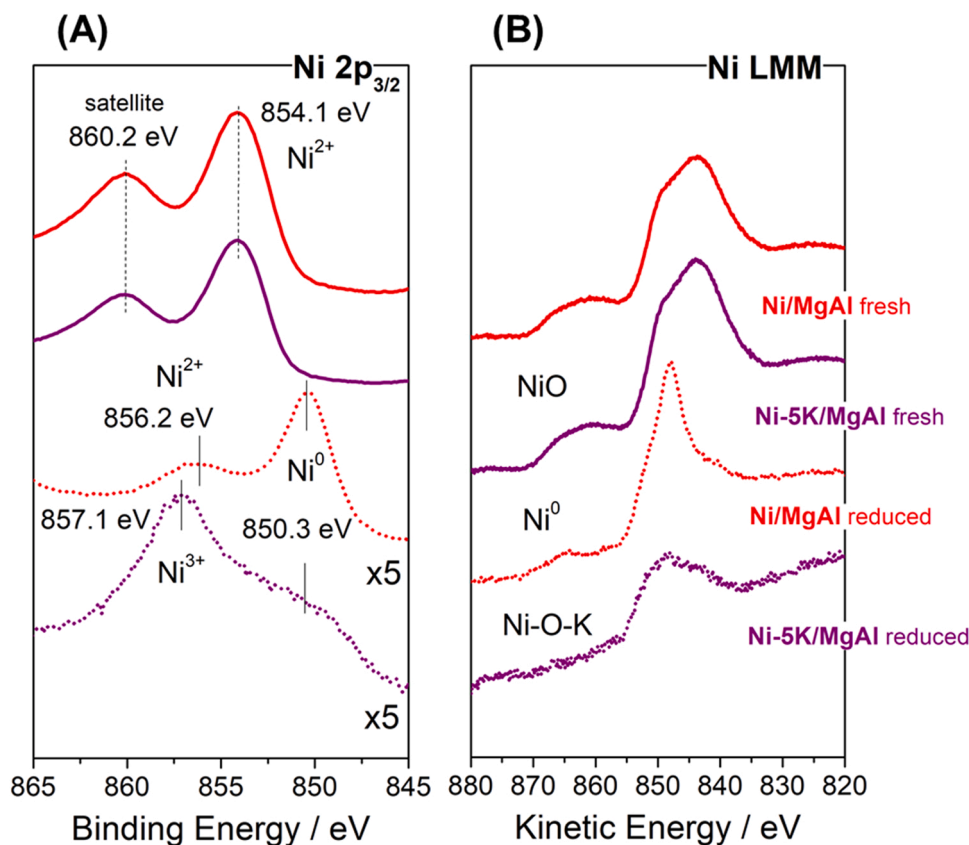
Fig. 4. Ni 2p$_{3/2}$ spectra (A) and Ni LMM Auger (B) of both Ni-MgAl and 5 K-Ni/MgAl samples without pretreatment and after reduction at 800 °C in hydrogen.

sample shows a Ni LMM Auger spectrum with a significant broad peak which can be fitted to NiOOH oxyhydroxides (*i.e.* Ni^{3+}), constituted by stacking faults with intercalated alkali cations [38,39]. Moreover, the confirmation of formation of a Ni-O-K oxide phase was also verified from the XPS spectra recorded in the K2p region for both fresh and reduced 5 K-Ni/MgAl samples. As illustrated in Fig. S2, the deconvolution of the K2p XPS spectra show that the reduced sample has two different potassium phases. This observation can be directly related to the formation of the Ni-O-K layer.

Based on these observations, we suggest that potassium interacts with nickel surface particles forming a core surrounded by a Ni-O-K phase (Ni@Ni-O-K). This phase likely presents an alkali-nickelate-type structure with nickel is stabilized in oxidation state + 3. In previous work, we demonstrated that CO is hardly adsorbed on K-promoted nickel catalysts [14]. Ni-O-K sites are accessible to hydrogen adsorption but not to CO adsorption. As discussed below, the importance of these sites in coke gasification is crucial for developing more stable dry reforming catalysts.

3.2. In situ study of Ni-O-K phase formation during reduction step: kinetic modelling

To gain additional insights on the origin of the new Ni-O-K phase, we conducted *in situ* DRIFT spectroscopy during a reduction experiment. Fig. 5 shows the evolution of the IR spectra recorded during the H$_2$-TPR reaction from room temperature to 750 °C for both Ni/MgAl and 5 K-Ni/MgAl samples, respectively. It also displays the evolution of the main gaseous species followed by MS as a function of time-on-stream and temperature for both samples.

With regards to the unpromoted Ni/MgAl sample (Fig. 5a), a complex set of bands attributable to polydentate (1510–1407 cm^{-1}), bidentate (1560–1360 cm^{-1}), and monodentate (1547–1373 cm^{-1}) carbonate species were initially detected in the 1600–1300 cm^{-1} region [14,40].

The bands at 1637 cm^{-1} and 3467 cm^{-1} are characteristic of physisorbed water. Early in the TPR, the release of physisorbed water leads to a band at 3730 cm^{-1}, characteristic of isolated hydroxyl species bound to tetrahedral Mg^{2+} cations on the MgAl$_2$O$_4$ surface [41]. The thermal stability of carbonate species increases from monodentate to polydentate species, and the most thermostable carbonates are only fully removed above 500 °C (Fig. 5b). All carbonate surface species were entirely removed by 750 °C. In agreement with this, the products detected by MS (Fig. 5c) include the release of H$_2$O and CO$_2$ in two steps at approximately 200 and 400 °C, suggesting the desorption of two types of labile carbonates. Above 500 °C, reduction of the most thermostable carbonate-like species was clearly accompanied by the formation of CH$_4$ and CO and the consumption of hydrogen.

On the other hand, the IR evolution for the 5 K-Ni/MgAl sample was significantly different to that of the unpromoted sample (Fig. 5d). Firstly, the spectra of 5 K-Ni/MgAl show that potassium addition completely neutralizes the hydroxyl surface species, in agreement with our previous work [14]. Consequently, multiple overlapping absorption bands were detected in the 1800–1200 cm^{-1} range at room temperature. At temperatures above 600 °C, most of these bands disappear and only the most thermostable species remain on the surface (Fig. 5e). These correspond to bulk polydentate or highly ionic carbonate species (1720–1407–1444 cm^{-1}), although monodentate carbonate species formed on very strong basic Mg-O-K sites (1584–1323 cm^{-1}) are also thermally stable [14,41,42]. Note that the presence of carbonate species on the samples likely stems from contact with CO$_2$ in air during preparation of the material (calcination), and this would be favored by the presence of basic potassium sites. On the other hand, not only labile carbonate species are removed during the reduction, but also nitrate species, observed in the 1550–1350 cm^{-1} region, disappear at temperatures between 500 and 600 °C. In terms of gases evolved during the reduction of 5 K-Ni/MgAl (Fig. 5f), an appreciable CO$_2$ and H$_2$O release is first observed without hydrogen consumption, indicating that labile
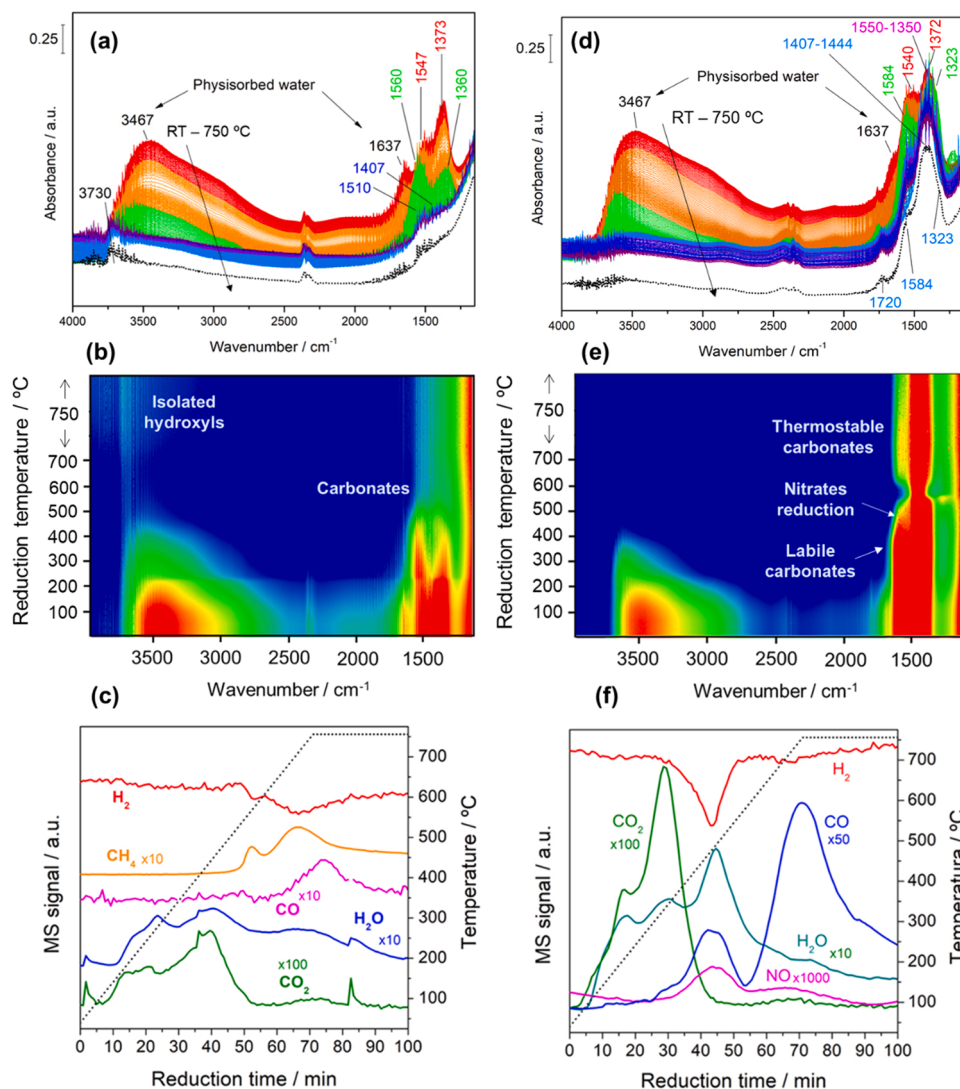
Fig. 5. DRIFTS spectra, 2D intensities contour map, and evolution profiles of gases detected on line by MS for both Ni/MgAl (a-c) and 5 K-Ni/MgAl (d-f) samples during *in situ* DRIFTS-MS reduction.

carbonates are decomposed into CO_2 and water below 400 °C. By contrast, an important hydrogen consumption was detected between 350 and 550 °C, peaking at 450 °C. This hydrogen depletion matches the production of NO, CO, and H_2O, corresponding to the reduction of nitrates and carbonates in this temperature range. Increasing the temperature further resulted in higher CO release, indicating that the reduction of carbonates by the reverse water gas shift reaction (RWGS) was accelerated above 600 °C. Notably, with this material, CH_4 was not detected at any temperature. Previous mechanistic studies suggested that adsorbed CO is an important reaction intermediate of CO_2 methanation [43]. The presence of Ni-O-K sites may inhibit CO adsorption and the subsequent production of methane.

A closer inspection of the IR spectra during reduction of 5 K-Ni/MgAl at 250–650 °C (Fig. 6) reveals the appearance of two bands at 2038 and 2158 cm^{-1} accompanied by the simultaneous decrease of the bands associated with bidentate carbonate species (1540 and 1372 cm^{-1}) and potassium nitrate-like species (1565, 1418, 1510 and 1363 cm^{-1}) [44]. The bands at 2038 cm^{-1}, observed between 250 and 450 °C, can be assigned to CO linearly adsorbed on small particles of metallic nickel, whereas the band at 2158 cm^{-1} had been assigned to linear NCO adsorbed forming cyanate-nickel complexes species [45]. However, we consider it is more reasonable to assign this band to nitrosyl(carbonyl) complexes formed on reduced nickel sites, given the CO and NO released

during the reduction. The formation of these nitrosyl(carbonyl) intermediates deserves attention since it allows to understand the formation of Ni-O-K sites.

The interaction between NiO particles and adsorbed potassium species is accompanied by an initial reduction of small particles of nickel oxide to metallic nickel, which begins at temperatures below 250 °C. The driving force of this step is the reduction of potassium carbonate species to generate highly stable alkali peroxide species and CO-linearly adsorbed on metallic nickel sites [37]. Under reducing conditions at 300–500 °C, potassium nitrate species are reduced, and a nitrosyl (carbonyl) complex is formed on reduced nickel sites. The thermal decomposition of this nitrosyl(carbonyl) intermediate occurs around 500 °C releasing CO and NO simultaneously. Presumably, the formation of the formally Ni^{3+} oxidation state evidenced by XPS can be attributed to the reduction of the alkali peroxide previously formed in the low temperature reduction. This step occurs at temperatures above 550 °C in which the oxygen of alkali peroxide is expended at high temperature to form trivalent alkali-nickelates (Ni-O-K sites). Fig. 6 sketches the plausible mechanism of formation of Ni-O-K sites. A similar process has also been proposed on the basis of FTIR studies of CO and adsorption experiments performed over analogous catalysts based on iron and potassium [46]. The authors hypothesized a similar mechanism to explain the formation of new phases ($KFeO_2$ and similar) constituted by oxidized
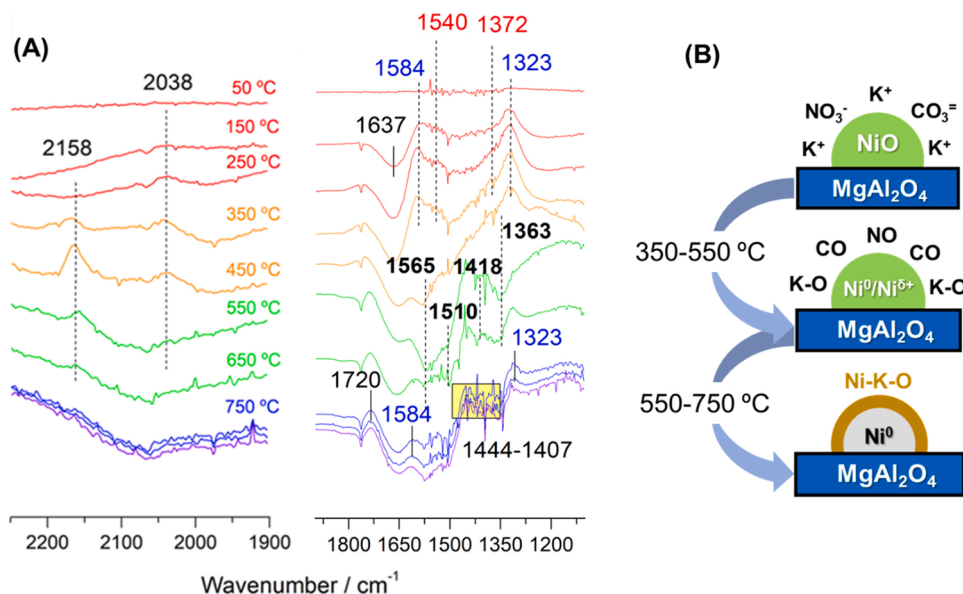
Fig. 6. (A) Evolution of difference IR spectra recorded as function of reduction temperature on 5 K-Ni/MgAl sample. For clarity purposes, the spectrum of the surface before reduction was subtracted from all the spectra. **(B)** Diagram of the Ni@Ni-O-K core-shell formation during reduction treatment.

iron and potassium in close contact. In agreement with the XRD and XPS results above, it is reasonable to assume that reduction of 5 K-Ni/MgAl catalyst at high temperature leads to the formation of an active phase composed of a metallic nickel core covered by Ni-O-K sites.

The modelling of H_2 temperature-programmed reduction (TPR) allows to evaluate the impact of potassium on the reducibility of the different materials. The H_2-TPR profiles for the materials are shown in Fig. 7. All samples display a broad reduction peak with multiple underlying components across the range 600–900 °C. We modelled the TPR process by considering three first-order reduction processes in an unsteady reactor model, resulting in a system of algebraic and ordinary differential equations (see Supporting Information for details). The resulting components fitted from the model are displayed in Fig. 7 and the corresponding parameters are included in Table S3. The three-component model recapitulates the TPR signal from the different materials very successfully and allows estimating the apparent activation energy for each reduction step (Fig. 7).

Potassium interacts with nickel and enhances its reducibility in the $Ni/MgAl_2O_4$ catalysts, as shown in Fig. 7. The TPR results indicate that the different reduction processes are initiated at lower temperatures as potassium loading is increased. This points to an interaction between nickel and potassium species (Fig. 7). The intermediate temperature component β (550–750 °C range) is associated with the reduction of NiO species with a moderate interaction with the support, whereas the component γ (> 750 °C) is assigned to the reduction of NiO_x complex species with a very strong metal-support interaction [47,48]. In fact, this high-temperature component can be associated with Ni^{2+} ions migrated into the $MgAl_2O_4$ matrix forming the non-stoichiometric nickel aluminate spinel ($NiAl_2O_4$) phase discussed above. Notably, the introduction of potassium above 3 wt% significantly increases the activation energy for the reduction of the γ component, indicating that potassium interacts with the $NiAl_2O_4$ phase and makes its reduction more temperature sensitive. The results also support the existence of a weaker interaction between K and NiO, with the activation energy for the reduction of NiO increasing slightly with K loading.

On the other hand, a reduction component α is observed below 500 °C, and its area under the curve notably increases with the potassium loading. Some authors have ascribed this reduction peak to bulk nickel oxide crystallites presenting very weak interactions with the support [49,50], and accordingly, it would indicate that a large amount

of nickel should be reduced in the 5 K-Ni/MgAl sample. However, this would be inconsistent with the characterization results above. Thus, to understand the origin of this peak, a MS spectrometer was coupled to analyze on line the gases released during the TPR process. As shown in Fig. S3, an intense peak of H_2 consumption around 420–430 °C was observed along with the formation of CO ($m/z= 28$), NO ($m/z= 30$) and H_2O ($m/z= 18$) in the samples with high potassium load. This indicates that the α component in the TPR results from the reduction of potassium nitrate and carbonate species. In addition, CO_2 ($m/z= 44$), CH_4 ($m/z= 15$), and CO ($m/z= 28$) were also detected during its reduction, and they decreased with the potassium loading (Fig. S3).

In summary, we conclude that Ni-O-K sites are not generated directly from the reaction of potassium oxide and nickel oxide on the K-Ni/$MgAl_2O_4$ catalysts but, instead, require an intermediate complex formed from potassium nitrate and carbonate species. These data provide additional evidence for the Ni-O-K phase. Ni-O-K sites seem available for hydrogen adsorption but not for CO adsorption.

3.3. Catalysts with Ni-O-K sites show superior stability in dry reforming reaction

To explore the functional implications of this new Ni-O-K phase, we investigated the catalytic performance of all prepared samples in dry reforming at 650 °C for 48 h, using different partial pressures of methane and CO_2 (20, 30 and 40 kPa) and a CH_4/CO_2 molar ratio equal to 1. Fig. 8 shows the CH_4 and CO_2 conversion over all the prepared catalysts against time-on-stream for the three partial pressures studied. Notably, Ni/MgAl and 1 K-Ni/MgAl catalysts suffered a drastic deactivation after 6 h when the reaction was performed at high partial pressures (30 and 40 kPa) of reactants. This was due to the rapid accumulation of coke, which even led to reactor plugging. It is well known that coke formation is related to CH_4 cracking and that dissociative adsorption of CH_x^* species is a rate-determining step sensitive to CH_4 partial pressure. By contrast, the catalysts promoted with high potassium loads showed stable CH_4 and CO_2 conversions during 48 h, even at high partial pressures of both reactants. This clearly indicates that potassium mitigates the carbon deposition or accelerates the gasification of carbon deposits.

Fig. S4 shows the evolution of the H_2/CO molar ratio over time during the tests performed at 20 kPa for all catalysts. The Ni/MgAl
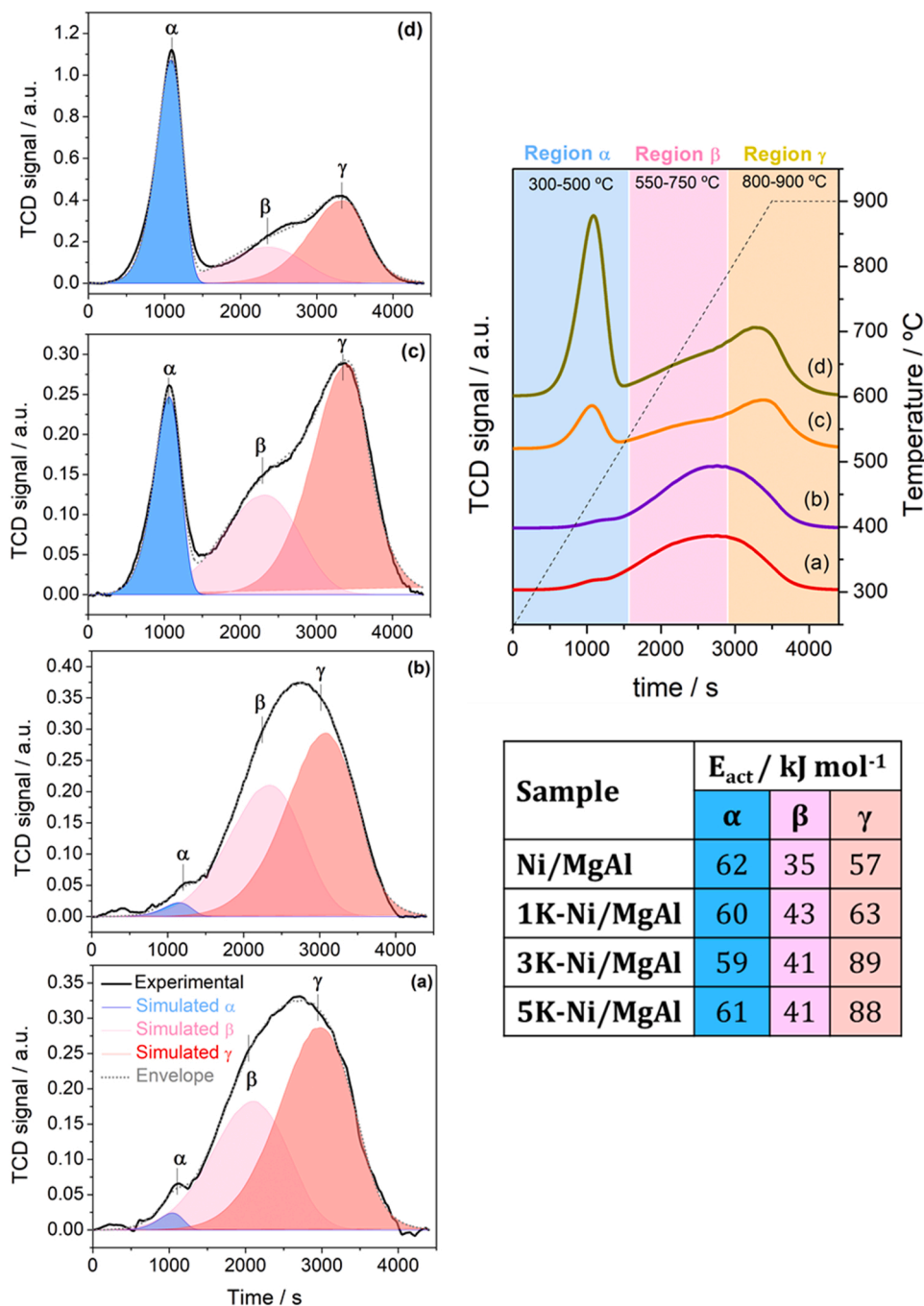
Fig. 7. H$_2$-TPR experimental and simulated profiles including the activation energy values calculated for (a) Ni/MgAl, (b) 1 K-Ni/MgAl, (c) 3 K-Ni/MgAl, and (d) 5 K-Ni/MgAl.

catalysts present a gradual increase of H$_2$/CO molar ratio over time, indicating that the unpromoted catalyst deactivates rapidly. Similarly, the Ni-1 K/MgAl catalyst shows an initial increase in the H$_2$/CO molar ratio, but it then stabilizes. This suggests that small amounts of K promote an equilibrium between the Boudouard reaction and carbon gasification, slowing catalyst deactivation. On the other hand, the H$_2$/CO ratios remain stable over time for the 3 K-Ni/MgAl and 5 K-Ni/MgAl catalysts. Both samples show H$_2$/CO molar ratios below the stoichiometric value of 1, pointing to stable carbon gasification and RWGS reactions. Consequently, no deactivation was observed for both potassium-rich catalysts. In agreement with these results, it has been reported that potassium promotes the RWGS reaction as it activates the CO$_2$ molecules *via* carbonates and subsequent reduction into CO [51, 52].

To quantify the amount of nickel exposed in the different materials, H$_2$ chemisorption experiments were carried out (Table 1). The results indicate that high potassium loads reduce the amount of exposed nickel sites. This may be due to i) the coverage of Ni sites by formation of a Ni-O-K layer and ii) the somewhat increased particle size (Fig. S8 and Table 1) upon K loading. The catalyst average particle sizes are slightly larger for samples with high potassium load. Some authors have reported an increased metal particle size upon addition of promoters such as Mg, K or Ce [53]. This suggests that potassium may favor the formation of larger nickel particles as a result of a weaker interaction with the MgAl$_2$O$_4$ support, in agreement with our TEM results (Fig. S5).

We also investigated the effect of potassium on the catalyst turnover
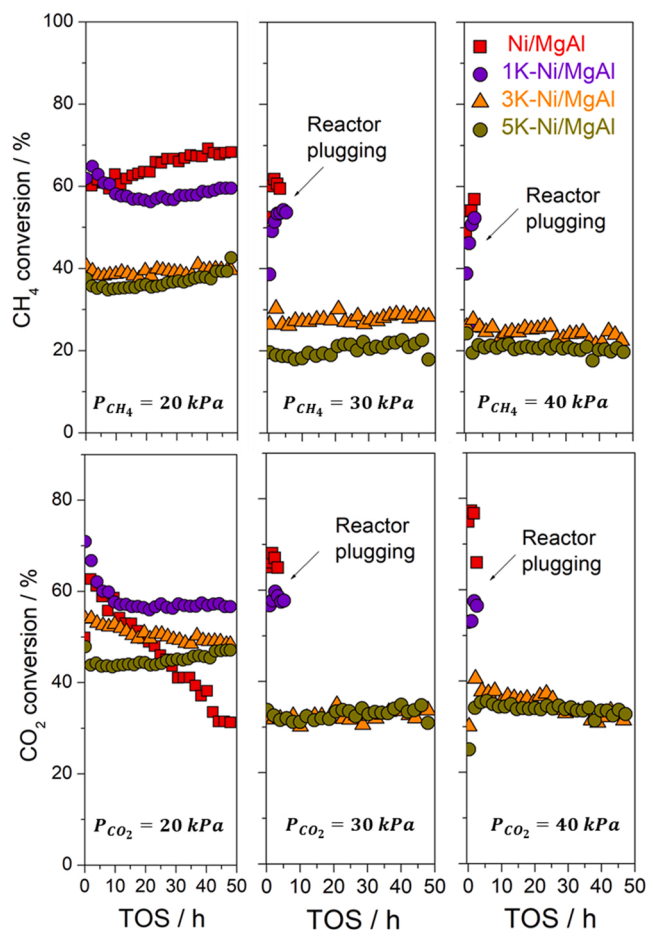
Fig. 8. Catalytic performance in terms of CO_2 and CH_4 conversion against time-on-stream at three partial pressures of both reactants (20, 30 and 40 kPa) at 650 °C and WHSV = 30 L g^{-1} h^{-1} with CH_4/CO_2 ratio equal to 1.

Table 1

Metal particle sizes were measured by TEM (Fig. S5, Supporting Information) and H_2 pulse chemisorption results were obtained for all the reduced catalysts. Catalytic activity was measured for all the catalysts during the first 10 min for dry reforming of methane at a partial pressure of both reactants of 20 kPa (CH_4: CO_2 = 1:1) at 650 °C and WHSV 30 L g^1 h^{-1}.

Samples	Ni particle size (nm)	Ni surface area exposed (m^2 g^{-1})	Nickel dispersion (%)	TOF CH_4 (s^{-1})	TOF CO_2 (s^{-1})
Ni /MgAl	12.5	24.3	3.7	0.084	0.091
1 K-Ni /MgAl	9.5	22.2	3.4	0.098	0.114
3 K-Ni /MgAl	16.5	3.5	0.54	0.419	0.545
5 K-Ni /MgAl	24	3.4	0.5	0.353	0.445

frequency (TOF), which expresses the activity of catalysts in terms of moles transformed per time unit and per mol of exposed nickel. Apparent TOF values were estimated from the run tests at 20 kPa using initial reaction rates and the dispersion of nickel estimated from H_2 chemisorption (Table 1). Notably, the samples containing 3 and 5 wt% K_2O displayed superior TOF values for both reactants. This indicates that, although the number of nickel sites exposed is reduced upon K addition, the C-H bond cleavage and the CO_2 activation in carbon gasification are greatly facilitated, consistent with the formation of a new Ni-O-K active phase.

In Fig. 9, the CH_4 and CO_2 consumption rates are compared with the H_2 and CO production rates, respectively, in terms of Ni metal surface exposed. As can be observed in Fig. 9A, CH_4 consumption and H_2 production rates are directly correlated with the Ni surface area exposed and thus Ni/MgAl and 1 K-Ni/MgAl catalyst, in which higher fraction of metallic nickel sites are exposed, favored these reactions. Likewise, the addition of potassium decreases the amount of exposed nickel sites due to the formation of Ni-O-K layer and both methane consumption and H_2 yield are less favored. On the other hand, Fig. 9B shows that CO_2 consumption and CO formation rate are also nickel structure-sensitive reactions. Remarkably, in the absence of potassium, the CO produced is significantly lower than the CO_2 consumed. When potassium is added, the CO produced matches the CO_2 consumed. This suggests that a sizeable proportion of CO produced on the unpromoted catalyst is dissociated to C* and O* species whereas, in the presence of Ni-O-K, CO does not adsorb and remains in the effluent. Therefore, the addition of potassium avoids the CO dissociation on nickel sites and thus decrease the accumulation of carbonaceous deposits. Moreover, this effect could open the door to enhanced low-temperature RWGS catalysts since CO dissociation favors the methanation reaction against reverse water gas shift reaction [54].

3.4. Carbon deposition: analysis of spent catalysts

Finally, the amount and nature of the carbon deposits after dry reforming of methane were studied as a function of potassium loading. The TPO profiles obtained for all samples are displayed in Fig. 10. The $m/z= 32$, $m/z= 44$, and $m/z= 28$ signals were chosen to analyze the evolution of O_2, CO_2, and CO, respectively. The area under a TPO profile is proportional to the amount of deposited carbon, and it is clearly seen that the 5 K-Ni/MgAl catalyst has the lowest amount of carbon deposited. As observed in Fig. 10, Ni/MgAl and 1 K-Ni/MgAl catalysts show maximal CO_2 production at 613 °C, which is associated with the oxidation of highly structured carbon species such as whiskers or carbon filamentous. This type of carbon is the main one responsible for pore blocking and metal particle encapsulation [10,55]. Note that there is an abrupt decline in the CO_2 signal on both Ni/MgAl and 1 K-Ni/MgAl catalysts at 716 °C and 750 °C. The amount of carbon deposited in these samples was so high that all oxygen of stream was fully consumed, and the CO_2 produced then reacted as an oxidant through the reverse Boudouard reaction (C* + CO_2 → CO). This explains the concurrent formation of CO gas. The TPO profiles obtained for 3 K-Ni/MgAl and 5 K-Ni/MgAl catalysts show that the carbon oxidation processes occur at
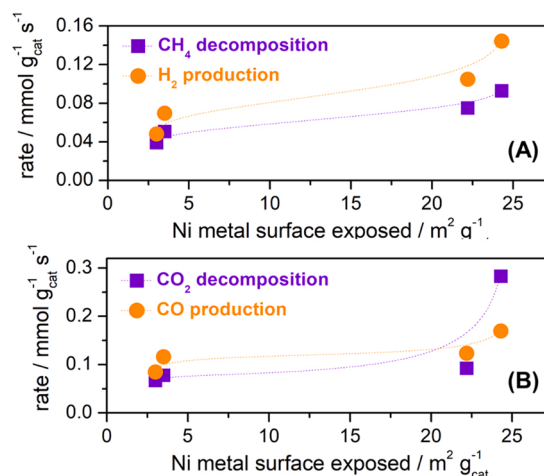

Fig. 9. (A) CH_4 consumption and H_2 production rates. **(B)** CO_2 consumption and CO production rates against surface area of nickel sites exposed for all catalyst in DRM reaction at partial pressure of both reactants of 20 kPa (CH_4/CO_2 = 1), 650 °C and GHSV = 30 L g^{-1} h^{-1}.
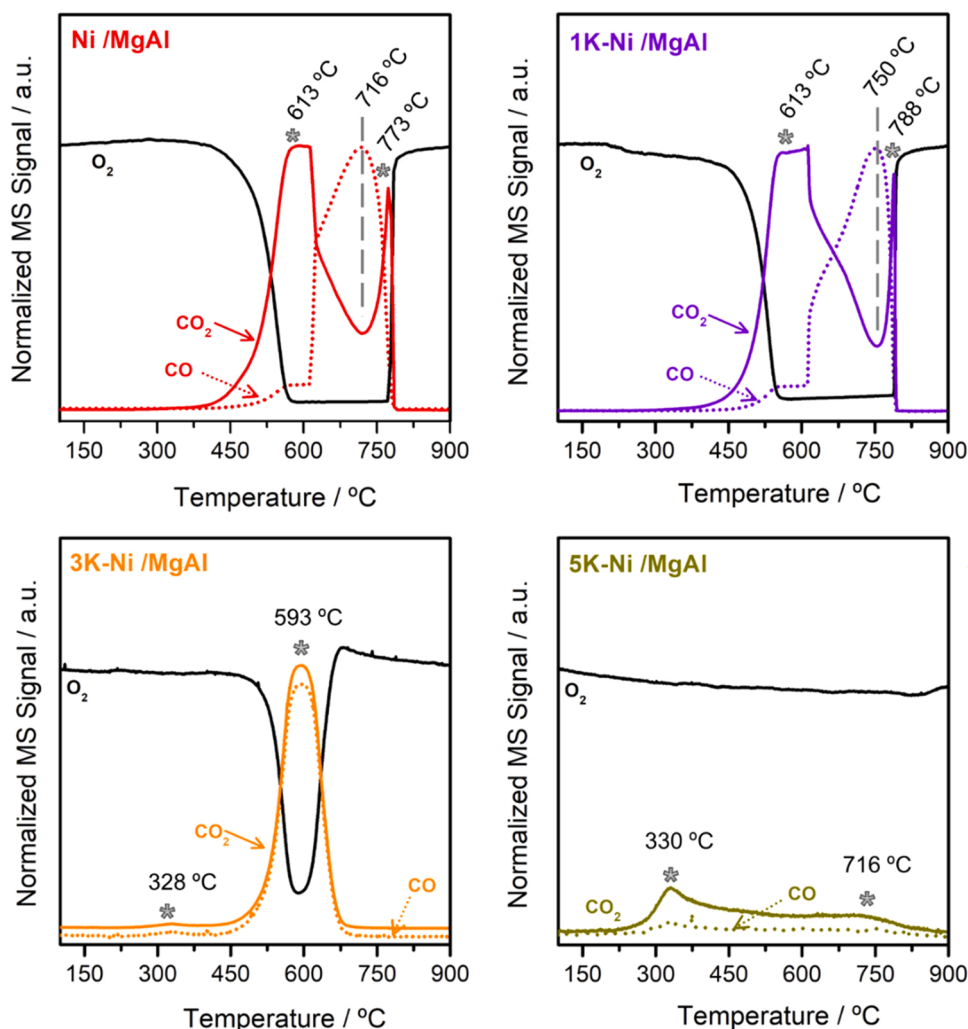
Fig. 10. TPO profiles of spent catalysts after 48 h of DRM reaction at partial pressure of both reactants of 20 kPa ($CH_4/CO_2 = 1$), 650 °C and GHSV = 30 L g^{-1} h^{-1}.

lower temperatures. The TPO profile of 3 K-Ni/MgAl catalyst peaks at 593 °C, consistent with the oxidation of carbon with a higher graphitic degree, probably small filamentous species [56]. The oxidation step occurring around 330 °C is ascribed to the oxidation of amorphous carbon, and this is the only process detected on the 5 K-Ni/MgAl spent catalyst.

Figs. S6 and S7 shows the structural analysis obtained by XRD and Raman spectroscopy, respectively, for all the spent catalysts. The XRD pattern (Fig. S6) obtained for Ni/MgAl spent catalyst present an intense and well-defined peak at $2\Theta = 26.5°$, associated with graphitic carbon species (JPDS 00-025-0284). This peak was less intense in the spent K-promoted catalysts, and it was absent in the Ni-5 K/MgAl sample. On the other hand, potassium loading increased the intensity of peaks associated with Ni^0, $MgAl_2O_4$ and Mg(Ni)O phases compared to the unpromoted sample.

The Raman spectra of Ni/MgAl, 1 K-Ni/MgAl and 3 K-Ni/MgAl catalysts, Fig. S7, are characterized by two main features at 1349 and 1578 cm^{-1}, ascribed to the vibrational modes D and G of carbon species, respectively. The D-band is characteristic of structurally disordered carbon while the G-band corresponds to C-C vibration stretching of structured carbon, such as graphite [57]. The D-to-G intensity ratio ($I_{(D/G)}$) is thus a valuable parameter to characterize the carbon disorder degree [58]. The $I_{(D/G)}$ ratios estimated for the spent catalysts follows the sequence 3 K-Ni/MgAl > 1 K-Ni/MgAl > Ni/MgAl (Fig. S7), indicating that potassium loading decreases the graphitization degree. These bands were absent in the 5 K-Ni/MgAl spent sample.

The morphology of spent catalysts was studied by SEM analysis (Fig. S8). As depicted in Fig. S4, the SEM micrographs show that the unpromoted catalyst becomes covered of carbon species with whisker or filamentous structure. Meanwhile, the amount of whisker carbon and the diameter of the filamentous decreases notably with the increment of potassium loading becoming wholly absent for 5 K-Ni/MgAl catalyst. These observations are consistent with the XRD and Raman spectroscopy results.

Taken together, the results reveal that, while the unpromoted catalyst became fully covered by carbonaceous deposits, increasing the loading of potassium led to less carbon deposition, which was also less graphitic in nature. Remarkably, deposits were fully prevented on the 5 K-Ni/MgAl catalyst, and its diffractogram coincides with the pattern of the reduced catalyst prior to reaction (Fig. 2), confirming an exceptional improvement in stability accompanying the new Ni-O-K phase.

4. Conclusions

The efficient conversion of biogas to syngas by dry reforming is a very promising route to produce liquid fuels, but low catalytic stability prevents its establishment as an industrial process. In this work, Ni-based catalysts promoted with potassium were tested in the dry reforming of methane and were exhaustively characterized to understand the key role of potassium in carbon deposition suppression. By means of different characterization techniques, we have established that, in the presence of 5 wt% of potassium, the nickel particles form a

core surrounded by a Ni-O-K inter-layer (Ni@Ni-O-K) during the reduction of the catalyst. Likely, this layer presents a structure type alkali-nickelate ($KNiO_2$), in which nickel is stabilized in oxidation state + 3. The Ni-O-K phase formation induces essential changes in the electronic properties of nickel. The presence of Ni-O-K sites leads to coke-resistant catalysts with excellent activity and stability. Specifically, these new sites do not catalyze the dissociation of CO, thus avoiding the formation of methane and coke and greatly enhancing the yield of syngas and the catalytic stability. The study also provides the first insights on the formation process of the Ni-O-K phase, providing a new direction to design high-performance dry reforming catalysts for sustainable syngas production.

Supporting Information

Textual properties; XPS K2p; TPR modeling details; SEM/TEM results; H_2/CO ratios results for DRM; Characterization of spent catalysts (XRD, Raman spectra and SEM); Figs. S1–S8 and Tables S1–S3.

CRediT authorship contribution statement

L. Azancot, V. Blay: Conceptualization, Methodology **L. Azancot, L.F. Bobadilla**: Data curation, Writing – original draft preparation. **V. Blay, R. Blay-Roger, L. Azancot, A. Penkova, M.A. Centeno**: Visualization, Investigation. **L.F. Bobadilla, J.A. Odriozola***: Supervision. **L. F. Bobadilla, L. Azancot:** Writing – review & editing, **J.A. Odriozola, M.A. Centeno***: Funding acquisition.

Author Contributions

The manuscript was written through contributions of all authors. All authors have given approval to the final version of the manuscript.

Declaration of Competing Interest

The authors declare that they have no known competing financial interests or personal relationships that could have appeared to influence the work reported in this paper.

Acknowledgment

Appendix A. Supporting information

Supplementary data associated with this article can be found in the online version at doi:10.1016/j.apcatb.2022.121148.

References

[1] A. Rafiee, K.R. Khalilpour, J. Prest, I. Skryabin, Biogas as an energy vector, Biomass Bioenergy 144 (2021), 105935.

[2] G. Vilardi, C. Bassano, P. Deiana, N. Verdone, Exergy and energy analysis of three biogas upgrading processes, Energy Convers. Manag. 224 (2020), 113323.

[3] D. Park, D.J. Moon, T. Kim, Steam-CO_2 reforming of methane on Ni/γ-Al2O3-deposited metallic foam catalyst for GTL-FPSO process, Fuel Process. Technol. 112 (2013) 28–34.

[4] A. Naqi, J.N. Kuhn, B. Joseph, Techno-economic analysis of producing liquid fuels from biomass via anaerobic digestion and thermochemical conversion, Biomass Bioenergy 130 (2019), 105395.

[5] A.H.K. Owgi, A.A. Jalil, I. Hussain, N.S. Hassan, H.U. Hambali, T.J. Siang, D.V. N. Vo, Catalytic systems for enhanced carbon dioxide reforming of methane: a review, Environ. Chem. Lett. 19 (2021) 2157–2183.

[6] Y. Wang, L. Yao, Y. Wang, S. Wang, Q. Zhao, D. Mao, C. Hu, Low-temperature catalytic CO_2 dry reforming of methane on Ni-Si/ZrO_2 catalyst, ACS Catal. 8 (2018) 6495–6506.

[7] Y. Song, E. Ozdemir, S. Ramesh, A. Adishev, S. Subramanian, A. Harale, M. Albuali, B.A. Fadhel, A. Jamal, D. Moon, S.H. Choi, C.T. Yavuz, Dry reforming of methane by stable Ni-Mo nanocatalysts on single-crystalline MgO, Science 367 (2020) 777–781.

[8] S.M. Kim, P.M. Abdala, T. Margossian, D. Hosseini, L. Foppa, A. Armutlulu, W. van Beek, A. Comas-Vives, C. Copéret, C. Müller, Cooperativity and dynamics increase the performance of NiFe dry reforming catalysts, J. Am. Chem. Soc. 139 (2017) 1937–1949.

[9] H. Topsøe, Developments in operando studies and in situ characterization of heterogeneous catalysts, J. Catal. 216 (2003) 155–164.

[10] A. Djaidja, S. Libs, A. Kiennemann, A. Barama, Characterization and activity in dry reforming of methane on NiMg/Al and Ni/MgO catalysts, Catal. Today 113 (2006) 194–200.

[11] D. Baudouin, U. Rodemerck, F. Krumeich, Ad Mallmann, K.C. Szeto, H. Ménard, L. Veyre, J.-P. Candy, P.B. Webb, C. Thieuleux, C. Copéret, Particle size effect in the low temperature reforming of methane by carbon dioxide on silica-supported Ni nanoparticles, J. Catal. 297 (2013) 27–34.

[12] T. Borowiecki, A. Denis, M. Rawski, A. Gołębiowski, K. Stolecki, J. Dmytrzyk, A. Kotarba, Studies of potassium-promoted nickel catalysts for methane steam reforming: effect of surface potassium location, Appl. Surf. Sci. 300 (2014) 191–200.

[13] F. Frusteri, L. Spadaro, F. Arena, A. Chuvilin, TEM evidence for factors affecting the genesis of carbon species on bare and K-promoted Ni/MgO catalysts during the dry reforming of methane, Carbon 40 (2002) 1063–1070.

[14] L. Azancot, L.F. Bobadilla, M.A. Centeno, J.A. Odriozola, IR spectroscopic insights into the coking-resistance effect of potassium on nickel-based catalyst during dry reforming of methane, Appl. Catal. B Environ. 285 (2021), 119822.

[15] L. Azancot, L.F. Bobadilla, J.L. Santos, J.M. Córdoba, M.A. Centeno, J.A. Odriozola, Influence of the preparation method in the metal-support interaction and reducibility of Ni-Mg-Al based catalysts for methane steam reforming, Int. J. Hydrog. Energy 44 (2019) 19827–19840.

[16] P. Makula, M. Pacia, W. Macyk, How to correctly determine the band gap energy of modified semiconductor photocatalysts based on UV–Vis spectra, J. Phys. Chem. Lett. 9 (2018) 6814–6817.

[17] A. Borodziński, M. Bonarowska, Relation between crystallite size and dispersion on supported metal catalysts, Langmuir 13 (1997) 5613–5620.

[18] Y. Wang, J.H. Zhu, W.Y. Huang, Synthesis and characterization of potassium-modified alumina superbases, Phys. Chem. Chem. Phys. 3 (2001) 2537–2543.

[19] M.Y. Nassar, I.S. Ahmed, I. Samir, A novel synthetic route for magnesium aluminate ($MgAl_2O_4$) nanoparticles using sol-gel auto combustion method and their photocatalytic properties, Spectrochim. Acta A Mol. Biomol. Spectrosc. 131 (2014) 329–334.

[20] J. Yan, J. Huang, T. Zhang, H. Tian, J. Yu, L. Zhang, Y. Zhang, Investigation of the microstructure, cation distribution and optical properties of nanoscale $NixMg1-xAl2O4$ spinel pigments, Ceram. Int. 45 (2019) 14073–14083.

[21] T. Sakurai, M. Ishigame, H. Arashi, Absorption spectrum of Ni^{2+} ions in spinel, J. Chem. Phys. 50 (1969) 3241–3245.

[22] K. Ullrich, S. Locmelis, M. Binnewies, K.D. Becker, An optical spectroscopy study of ionic defects: Ni^{2+} ions in tetrahedral coordination, Phase Transit. 76 (2003) 103–116.

[23] L. D'Amario, J. Föhlinger, G. Boschloo, L. Hammarström, Unveiling hole trapping and surface dynamics of NiO nanoparticles, Chem. Sci. 9 (2018) 223–230.

[24] S. Sawai, T. Uchino, Visible photoluminescence from $MgAl_2O_4$ spinel with cation disorder and oxygen vacancy, J. Appl. Phys. 112 (2012) 103523.

[25] P.D. Borges, J. Cott, F.G. Pinto, J. Tronto, L. Scolfaro, Native defects as sources of optical transitions in $MgAl_2O_4$ spinel, Mater. Res. Express 3 (2016), 076202.

[26] F. Wrobel, H. Shin, G.E. Sterbinsky, H.-W. Hsiao, J.-M. Zuo, P. Ganesh, J.T. Krogel, A. Benali, P.R.C. Kent, O. Heinonen, A. Bhattacharya, Local structure of potassium doped nickel oxide: a combined experimental-theoretical study, Phys. Rev. Mater. 3 (2019), 115003.

[27] H. Müller-Buschbaum, Zur Kristallchemie von oxoniccolaten der Alkali-, Erdalkali- und Seltenerdmetalle, Z. Anorg. Allg. Chem. 637 (2011) 797–820.

[28] M.A. Hitchman, H. Stratemeier, R. Hoppe, Electronic and Raman spectra of the linear dioxonickilate(2-) ion in dipotassium dioxonickalate(2-), Inorg. Chem. 27 (1988) 2506–2510.

[29] W.D. Mross, Alkali doping in heterogeneous catalysis, Catal. Rev. 25 (1983) 591–637.

[30] G.A. El-Shobaky, N.S. Petro, Effect of doping on the sintering of finely divided NiO catalyst, Surf. Technol. 13 (1981) 197–203.

[31] H. Praliaud, M. Primet, G.-A. Martin, Physico-chemical properties of potassium-promoted Ni/SiO_2 catalysts, Appl. Surf. Sci. 17 (1983) 107–123.

[32] H. Kim, D.-H. Seo, A. Urban, J. Lee, D.-H. Kwon, S.-H. Bo, T. Shi, J.K. Papp, B. D. McCloskey, G. Ceder, Stoichiometric layered potassium transition metal oxide for rechargeable potassium batteries, Chem. Mater. 30 (2018) 6532–6539.

[33] A.M. Tarditi, N. Barroso, A.E. Galetti, L.A. Arrúa, L. Cornaglia, M.C. Abello, XPS study of the surface properties and Ni particle size determination of Ni-supported catalysts: surface properties and Ni particle size determination of Ni catalysts, Surf. Interface Anal. 46 (2014) 521–529.

[34] J. Shen, A.A.C. Reule, N. Semagina, Ni/$MgAl_2O_4$ catalyst for low-temperature oxidative dry methane reforming with CO_2, Int. J. Hydrog. Energy 44 (2019) 4616–4629.

[35] A.P. Grosvenor, M.C. Biesinger, R.S.C. Smart, N.S. McIntyre, New interpretations of XPS spectra of nickel metal and oxides, Surf. Sci. 600 (2006) 1771–1779.

[36] D. Soo Kim, H. Chul Lee, Nickel vacancy behavior in the electrical conductance of nonstoichiometric nickel oxide film, J. Appl. Phys. 112 (2012), 034504.

[37] A.F. Carley, S.D. Jackson, J.N. O'Shea, M.W. Roberts, The formation and characterisation of Ni^{3+} — an X-ray photoelectron spectroscopic investigation of potassium-doped Ni(110)–O, Surf. Sci. 440 (1999) L868–L874.

[38] M.C. Biesinger, L.W.M. Lau, A.R. Gerson, R.S.C. Smart, The role of the Auger parameter in XPS studies of nickel metal, halides and oxides, Phys. Chem. Chem. Phys. 14 (2012) 2434–2442.

[39] L. Eriksson, U. Palmqvist, H. Rundlöf, U. Thuresson, R. Sjövall, Structural aspects on the charged positive Ni electrode, J. Power Sources 107 (2002) 34–41.

[40] G. Busca, V. Lorenzelli, Infrared spectroscopic identification of species arising from reactive adsorption of carbon oxides on metal oxide surfaces, Mater. Chem. 7 (1982) 89–126.

[41] C. Morterra, G. Ghiotti, F. Boccuzzi, S. Coluccia, An infrared spectroscopic investigation of the surface properties of magnesium aluminate spinel, J. Catal. 51 (1978) 299–313.

[42] J.I. Di Cosimo, V.K. Díez, M. Xu, E. Iglesia, C.R. Apesteguía, Structure and surface and catalytic properties of Mg-Al basic oxides, J. Catal. 178 (1998) 499–510.

[43] Y. Yang, J. Liu, F. Liu, D. Wu, Reaction mechanism of CO$_2$ methanation over Rh/TiO$_2$ catalyst, Fuel 276 (2020), 118093.

[44] D.H. Kim, K. Mudiyanselage, J. Szányi, H. Zhu, J.H. Kwak, C.H.F. Peden, Characteristics of Pt–K/MgAl$_2$O$_4$ lean NO$_x$ trap catalysts, Catal. Today 184 (2012) 2–7.

[45] L. Wang, S. Zhu, N. Marinkovic, S. Kattel, M. Shao, B. Yang, J.G. Chen, Insight into the synergistic effect between nickel and tungsten carbide for catalyzing urea electrooxidation in alkaline electrolyte, Appl. Catal. B Environ. 232 (2018) 365–370.

[46] E. Guglielminotti, F. Boccuzzi, F. Pinna, G. Strukul, The effect of potassium addition on the surface chemical structure and activity of supported iron, J. Catal. 167 (1997) 153–163.

[47] O.W. Pérez-López, A. Senger, N.R. Marcilio, M.A. Lansarin, Effect of composition and thermal pretreatment on properties of Ni–Mg–Al catalysts for CO$_2$ reforming of methane, Appl. Catal. A Gen. 303 (2006) 234–244.

[48] H. Özdemir, M.A.F. Öksüzömer, M.A. Gürkaynak, Effect of the calcination temperature on Ni/MgAl$_2$O$_4$ catalyst structure and catalytic properties for partial oxidation of methane, Fuel 116 (2014) 63–70.

[49] J. Juan-Juan, M.C. Román-Martínez, M.J. Illán-Gómez, Effect of potassium content in the activity of K-promoted Ni/Al$_2$O$_3$ catalysts for the dry reforming of methane, Appl. Catal. A Gen. 301 (2006) 9–15.

[50] C.S. Chen, J.H. Lin, J.H. You, K.H. Yang, Effects of potassium on Ni-K/Al$_2$O$_3$ catalysts in the synthesis of carbon nanofibers by catalytic hydrogenation of CO$_2$, J. Phys. Chem. A 114 (2010) 3773–3781.

[51] X. Yang, X. Su, X. Chen, H. Duan, B. Liang, Q. Liu, X. Liu, Y. Ren, Y. Huang, T. Zhang, Promotion effects of potassium on the activity and selectivity of Pt/zeolite catalysts for reverse water gas shift reaction, Appl. Catal. B Environ. 216 (2017) 95–105.

[52] B. Liang, H. Duan, X. Su, X. Chen, Y. Huang, X. Chen, J.J. Delgado, T. Zhang, Promoting role of potassium in the reverse water gas shift reaction on Pt/mullite catalyst, Catal. Today 281 (2017) 319–326.

[53] Y.X. Zeng, L. Wang, C.F. Wu, J.Q. Wang, B.X. Shen, X. Tu, Low temperature reforming of biogas over K-, Mg- and Ce-promoted Ni/Al$_2$O$_3$ catalysts for the production of hydrogen rich syngas: understanding the plasma-catalytic synergy, Appl. Catal. B Environ. 224 (2018) 469–478.

[54] M. Roiaz, E. Monachino, C. Dri, M. Greiner, A. Knop-Gericke, R. Schlögl, G. Comelli, E. Vesselli, Reverse water-gas shift or sabatier methanation on Ni(110)? Stable surface species at near-ambient pressure, J. Am. Chem. Soc. 138 (2016) 4146–4154.

[55] I. Luisetto, S. Tuti, C. Battocchio, S. Lo Mastro, A. Sodo, Ni/CeO$_2$–Al$_2$O$_3$ catalysts for the dry reforming of methane: The effect of CeAlO$_3$ content and nickel crystallite size on catalytic activity and coke resistance, Appl. Catal. A Gen. 500 (2015) 12–22.

[56] Z. Alipour, M. Rezaei, F. Meshkani, Effect of alkaline earth promoters (MgO, CaO, and BaO) on the activity and coke formation of Ni catalysts supported on nanocrystalline Al$_2$O$_3$ in dry reforming of methane, J. Ind. Eng. Chem. 20 (2014) 2858–2863.

[57] C. Anjaneyulu, G. Naresh, V.V. Kumar, J. Tardio, T.V. Rao, A. Venugopal, Influence of rare earth (La, Pr, Nd, Gd, and Sm) metals on the methane decomposition activity of Ni–Al catalysts, ACS Sustain. Chem. Eng. 3 (2015) 1298–1305.

[58] S. Cimino, L. Lisi, G. Mancino, Effect of phosphorous addition to Rh-supported catalysts for the dry reforming of methane, Int. J. Hydrog. Energy 42 (2017) 23587–23598.